Path Integral Monte Carlo Calculation of the Momentum Distribution of the Homogeneous Electron Gas at Finite Temperature

B. Militzer[a], E. L. Pollock[b], D. M. Ceperley[c]

[a]*Department of Earth and Planetary Science, Department of Astronomy, University of California, Berkeley, CA 94720*
[b]*Lawrence Livermore National Laboratory, University of California, Livermore, CA 94550*
[c]*Department of Physics, University of Illinois at Urbana-Champaign, Urbana, IL 61801*

Abstract

Path integral Monte Carlo (PIMC) simulations are employed to calculate the momentum distribution of the homogeneous electron gas at finite temperature. Open paths are introduced to sample off-diagonal elements of the real-space density matrix. It is demonstrated how the restricted PIMC method can be extended to incorporate open paths in order to allow for the simulations in fermionic systems where a sign problem is present. The computed momentum distribution shows significant deviations from behavior of free fermions when strong correlations are present but agrees with predictions from variational methods.

Keywords: path integral Monte Carlo, momentum distributions, first-principles simulations, dense plasmas

1. Introduction

The momentum distribution is one of the fundamental properties of a quantum system. It can be directly measured by inelastic scattering or by recording the trajectories of particles. The first method has been used to determine the condensate fraction in superfluid helium while the latter was used to demonstrate that Bose-Einstein condensation of supercooled alkali atoms in magnetic traps had been achieved.

In this article, we calculate the momentum distribution of interacting fermions at finite temperature with restricted path integral Monte Carlo (PIMC) simulations. We will illustrate how the fermionic momentum distribution evolves as a function of temperature. At high temperature well above the Fermi temperature, T_F, the momentum distribution very closely resembles a Maxwell-Boltzmann distribution. With decreasing temperature, Pauli exclusion effects become important and the Fermi-Dirac distribution must instead be employed. While it is straightforward to study this transition in systems

of noninteracting particles with analytical methods [1], the derivation of the momentum distribution of interacting bosons and fermions typically relies on computer simulations. Interacting bosons (^{4}He) at finite temperature have been studied with PIMC simulations previously [2]. Ground state quantum Monte Carlo simulations have been employed to derive the momentum distribution of the homogeneous electron gas at zero temperature [3]. In this article, we use PIMC simulations to perform such calculations at finite temperature. It is the combination of fermionic and interaction effects that make this a challenging calculation. Conversely for systems of classical particles, the degrees of freedom in coordinate and momentum space can be separated and Maxwell-Boltzmann momentum distribution emerges regardless of the interactions. For quantum systems, this separation is no longer possible because the position and momentum operators do not commute. That is why we employ PIMC simulations in this article to derive the momentum distribution of interacting electrons.

Since momentum and positions are conjugate variables in quantum mechanics, it is necessary to introduce *open paths* to sample off-diagonal density matrix elements needed for the momentum distribution. We discuss how the restricted path method can be extended to simulations with open paths. While all negative signs can be eliminated from fermionic simulations with closed paths, some negative contributions are unavoidable in simulations with open paths. However, the simulations are stable and signal-to-noise ratio remains high for all temperatures under consideration. We illustrate how the momentum distribution gradually changes from Maxwell-Boltzmann to Fermi-Dirac type with decreasing temperature. We find that correlations among the electrons prevent an ideal Fermi step function from emerging in the limit of low temperature because plane waves are not the eigenstates of a system of interacting particles. We performed simulations at two different densities to illustrate how strongly the correlation effects affect the momentum distribution.

2. Path integral Monte Carlo

The basic techniques for simulating bosonic quantum systems of bosons was developed in Ref. [4] and reviewed in Ref. [2]. Subsequently the algorithm was generalized to fermion systems using the restricted path integral method. The first results of this simulation method were reported in the seminal work on liquid ^{3}He[5] and dense hydrogen [6]. A review of the algorithm is given in Ref. [7]. In subsequent articles, this method was applied to study hydrogen [8, 9, 10, 11, 12], helium [13, 14, 15], hydrogen-helium mixtures [16] and one-component plasmas [17, 18, 19]. Recent work on the one-component plasma using this and related methods were presented in [20, 21, 22, 23]. In recent years the method was extended to simulate plasmas of various first-row elements [24, 25, 26, 27, 28, 29] and with the development of Hartree-Fock nodes, the simulations of second-row elements became possible [30, 31, 32, 33].

In PIMC simulations of thermodynamic properties, one only samples the diagonal elements of the many-body density matrix. Such calculations involve *closed paths* in imaginary time. Following the procedure developed for the computation of the momentum distribution of bosonic systems [2], we extend this approach to restricted path simulations for fermions. Similarly the momentum distribution is obtained by sampling off-diagonal elements of the many-body density matrix. This requires PIMC simulations

with *one open path*. We explain how this path is sampled efficiently, which permutations need to be considered and how the path restriction is applied.

2.1. Restricted paths technique

The thermodynamic properties of a quantum many-body system can be derived from the thermal density, $\hat{\rho} = e^{-\beta\hat{\mathcal{H}}}$ with $\beta = 1/k_b T$. For the purpose of performing Monte Carlo simulations, we express this operator in position space,

$$\rho(\mathbf{R}, \mathbf{R}'; \beta) \equiv \langle \mathbf{R} | \hat{\rho} | \mathbf{R}' \rangle = \sum_s e^{-\beta\epsilon_s} \Psi_s^*(\mathbf{R}) \Psi_s(\mathbf{R}') \,, \tag{1}$$

where Ψ_s are the many-body eigenfunctions and ϵ_s the corresponding eigenvalues. $\mathbf{R} = \{\mathbf{r}_1, \ldots, \mathbf{r}_N\}$ represents a set of coordinates of N particles in d dimensions. The density matrix of a bosonic (B) or fermionic (F) system, $\rho_{\mathrm{B/F}}(\mathbf{R}, \mathbf{R}'; \beta)$, can be constructed from the density matrix for distinguishable particles (D) by a sum of permutations, $\mathcal{P}$, to project out states of the corresponding symmetry,

$$\rho_{\mathrm{B/F}}(\mathbf{R}, \mathbf{R}'; \beta) = \frac{1}{N!} \sum_{\mathcal{P}} (\pm 1)^{\mathcal{P}} \rho_{\mathrm{D}}(\mathbf{R}, \mathcal{P}\mathbf{R}'; \beta) \,, \tag{2}$$

where $(\pm 1)^{\mathcal{P}}$ denotes the sign of the permutation. Using the operator identity, $e^{-\beta\hat{\mathcal{H}}} = (e^{-\tau\hat{\mathcal{H}}})^M$, the density matrix at temperature T can be expressed in terms of density matrices at a higher temperature MT. This leads to a path integral in imaginary time with M steps of size $\tau = \beta/M$,

$$\begin{aligned}
\rho_{\mathrm{B/F}}(\mathbf{R}, \mathbf{R}'; \beta) &= \frac{1}{N!} \sum_{\mathcal{P}} (\pm 1)^{\mathcal{P}} \int \ldots \int d\mathbf{R}_1 \, d\mathbf{R}_2 \ldots d\mathbf{R}_{M-1} \\
&\quad \rho_{\mathrm{D}}(\mathbf{R}, \mathbf{R}_1; \tau) \, \rho_{\mathrm{D}}(\mathbf{R}_1, \mathbf{R}_2; \tau) \ldots \rho_{\mathrm{D}}(\mathbf{R}_{M-1}, \mathcal{P}\mathbf{R}'; \tau) \\
&= \frac{1}{N!} \sum_{\mathcal{P}} (\pm 1)^{\mathcal{P}} \int_{\mathbf{R} \to \mathcal{P}\mathbf{R}'} d\mathbf{R}_t \; e^{-S[\mathbf{R}_t]} \,, \tag{3}
\end{aligned}$$

where S represents the action of the path $\mathbf{R}_t$ beginning at $\mathbf{R}$ and ending at $\mathcal{P}\mathbf{R}'$. In calculations reported here we use the pair density matrix [4, 34, 35] for the action arising from the pair potentials. For bosonic many-body systems, the integrand is nonnegative and this expression can be efficiently evaluated using Monte Carlo techniques [4, 36, 2]. For fermions, a straightforward evaluation of this expression is impractical because there are many positive and negative contribution that nearly cancel. While one can still use this expression to numerically study systems of a few fermions, the efficiency rapidly decays with increasing number of particles and decreasing temperature, $\sim e^{-\beta N}$. This is referred to as the *fermion sign problem*.

In Refs. [37, 5, 7], it was shown that the fermion sign problem in imaginary time path integrals can be solved by *restricting* the path integration to a subset of the entire configuration space. One introduces the concept of fermion *nodes* that present the surface where the fermion many-body density matrix vanishes, $\rho_F(\mathbf{R}, \mathbf{R}'; t) = 0$. The nodes are employed to confine the paths, $\mathbf{R}(t)$, to regions where the density matrix is nonzero, $\rho_F(\mathbf{R}^*, \mathbf{R}(t); t) \neq 0$. $\mathbf{R}^*$ is called the *reference point*. It defines the allowed region,

$\Upsilon(\mathbf{R}^*)$, for the paths to travel in $\{\mathbf{R}, t\}$ space. The fermionic density matrix is then given by the restricted path integral,

$$\rho_F(\mathbf{R}^*, \mathbf{R}'; \beta) = \frac{1}{N!} \sum_{\mathcal{P}} (-1)^{\mathcal{P}} \int_{\mathbf{R}(t)=\mathbf{R}^* \to \mathcal{P}\mathbf{R}' \in \Upsilon(\mathbf{R}^*)} \mathbf{dR}_t \; e^{-S[\mathbf{R}_t]} \quad , \tag{4}$$

where one sums over all permutation of identical particles and integrates over all paths that do not cross the nodes. By introducing this nodal restriction, one effectively cancels negative and positive contributions to the path integral. When diagonal matrix elements are computed, all negative contributions are cancelled against a subset of the positive contributions. Thus only positive contributions remain to enter the calculation of thermodynamic averages $\langle \mathcal{O} \rangle$, like pressure, kinetic, potential and internal energy as well as pair correlation functions:

$$\langle \mathcal{O} \rangle = \frac{1}{\mathcal{Z}} \int \mathbf{dR} \, \rho(\mathbf{R}, \mathbf{R}; \beta) \, \langle \mathbf{R} | \, \mathcal{O} \, | \mathbf{R} \rangle \, , \tag{5}$$

$$\mathcal{Z} = \int \mathbf{dR} \, \rho(\mathbf{R}, \mathbf{R}; \beta) \quad . \tag{6}$$

Such computations require only simulations with closed paths that originate from a point $\mathbf{R}$ and terminate at the original or permuted set of coordinates, $\mathcal{P}\mathbf{R}$. The nodal restriction eliminates all contributions from odd permutations, which would otherwise enter with negative weights, because their paths violate the nodal restriction an odd number of times.

A complete cancellation of the negative terms is only achieved for the computation of diagonal density matrix elements. For the calculation of off-diagonal elements, some negative contributions enter even into the restricted path method. Nevertheless the weight of these contributions is much less than that of the positive terms as we will illustrate below. The restriction gives rise to an efficient numerical algorithm that scales favorably with increasing number of particles, similar to that for bosons.

The expression in Eq. 4 is exact as long as the nodes of the density matrix are known exactly [37]. However, the many-body density matrix is only known in a few cases, e.g. for noninteracting particles. In practice, one introduces a *trial* density matrix $\rho_\mathrm{T}(\mathbf{R}, \mathbf{R}'; \beta)$ in order to approximate the nodes of the real fermionic density matrix. This introduces an uncontrolled approximation into the calculation of all observables. However, for many fermionic systems this technique has been shown to work well.

The standard form of the fermionic trial density matrix is a Slater determinant of single particle density matrices,

$$\rho_T(\mathbf{R}, \mathbf{R}'; \beta) = \begin{vmatrix} \rho^{[1]}(\mathbf{r}_1, \mathbf{r}'_1; \beta) & \dots & \rho^{[1]}(\mathbf{r}_N, \mathbf{r}'_1; \beta) \\ \dots & \dots & \dots \\ \rho^{[1]}(\mathbf{r}_1, \mathbf{r}'_N; \beta) & \dots & \rho^{[1]}(\mathbf{r}_N, \mathbf{r}'_N; \beta) \end{vmatrix} \quad . \tag{7}$$

Often one neglects the interactions when the single particle density matrices are derived

$$\rho_0^{[1]}(\mathbf{r}, \mathbf{r}'; \beta) = (4\pi\lambda\beta)^{-d/2} \exp\left\{ -\frac{(\mathbf{r} - \mathbf{r}')^2}{4\lambda\beta} \right\} \quad , \tag{8}$$

4

where $\lambda = \hbar^2/2m$. However, PIMC simulations with variational [38] and Hartree-Fock nodes [30] have also been performed. Interaction effects can be introduced with the backflow method [37, 7].

At high temperature, interaction effects are small and the free particle nodes provide a very accurate representation of the nodal structure. With decreasing temperature, interaction effects become more important and consequently the error increases that results from employing free particle nodes [10]. One can improve the nodal approximation by using the dual-reference point method [7] that we will use throughout this work. In this approach, the time argument in the nodal restriction, $\rho_T(\mathbf{R}^*, \mathbf{R}(t); t^*) \neq 0$ is modified to become the smallest difference in imaginary time to the reference point, $t^* = \min(t, \beta - t)$.

How sensitive the computed thermodynamic averages are to the type of nodal approximation depends on the magnitude of the interactions in the system under consideration. Generally, one expects free particle nodes to work very well at high temperature and if correlation effects are weak. Also, when particles are localized like the electrons in molecular hydrogen or particles in a Wigner crystal, the effect of the nodes is reduced and the type of nodal restriction is not important.

An additional approximation arises from the evaluation of the action for a non-zero time-step $\tau > 0$ with an assumed restriction. The restriction has the form of a many-body (i.e. not pairwise) hard wall potential. Simply rejecting node-crossing paths (the primitive approximation) leads to an error in the energy of order $\tau^{1/2}$. We use an approximate form of the action based on the image method [7]. The distance of the path from the node is calculated using a Newton estimate. With this form for the fermion action, the kinetic energy has an error of order $\tau^{3/2}$ and is quite large for weakly correlated systems such as the electron gas for small r_s. Other quantities, such as the single particle density matrix are much less sensitive to this time-step error.

2.2. Computation of the momentum distribution

The single-particle momentum distribution for N_σ particles in spin state, σ, is defined as,

$$n_\sigma(\mathbf{k}) = \frac{(2\pi\hbar)^d}{\Omega} \left\langle \sum_{j=1}^{N_\sigma} \delta(\hat{\mathbf{p}}_j - \hbar\mathbf{k}) \right\rangle , \qquad (9)$$

where Ω is the volume of the simulation cell. The normalization for a finite system and in the thermodynamic limit respectively is given by,

$$\sum_{\mathbf{k}} n(\mathbf{k}) = N_\sigma \quad , \quad \frac{\Omega}{(2\pi)^d} \int d\mathbf{k}\, n(\mathbf{k}) = N_\sigma . \qquad (10)$$

Inserting $\langle \mathbf{R}|\mathbf{P}\rangle = e^{-i\mathbf{R}\cdot\mathbf{P}/\hbar}/(2\pi\hbar)^{Nd/2}$, one finds,

$$n(\mathbf{k}) = \frac{1}{\mathcal{Z}\Omega} \int d\mathbf{R}d\mathbf{R}'d\mathbf{P}\, \langle \mathbf{R}|\hat{\rho}|\mathbf{R}'\rangle \frac{e^{i\mathbf{P}\cdot(\mathbf{R}-\mathbf{R}')/\hbar}}{(2\pi\hbar)^{(N-1)d}} \sum_{j=1}^{N_\sigma} \delta(\mathbf{p}_j - \hbar\mathbf{k}) \qquad (11)$$

$$= \frac{N_\sigma}{\mathcal{Z}\Omega} \int d\mathbf{R}d\mathbf{r}_1'\, e^{i(\mathbf{r}_1 - \mathbf{r}_1')\cdot\mathbf{k}} \rho(\mathbf{r}_1, \ldots, \mathbf{r}_N, \mathbf{r}_1', \mathbf{r}_2, \ldots, \mathbf{r}_N). \qquad (12)$$

We assumed all particles are equivalent and particle 1 has spin σ. Consequently, $n(\mathbf{k})$ is given by the Fourier transform of the single-particle reduced density matrix (SPRDM),

$n(\mathbf{s})$,

$$n(\mathbf{k}) \;=\; \frac{N_\sigma}{\Omega} \int \mathbf{ds}\, e^{-i\mathbf{ks}}\, n(\mathbf{s}) \;, \tag{13}$$

$$n(\mathbf{s}) \;=\; \frac{1}{\mathcal{Z}} \int \mathbf{dR}\, \rho(\mathbf{r}_1, \mathbf{r}_2, \ldots, \mathbf{r}_N\,,\, \mathbf{r}_1 + \mathbf{s}, \mathbf{r}_2, \ldots, \mathbf{r}_N) \;. \tag{14}$$

Note that by the definition $n(s=0)$ equals 1.

Classical particles have a Maxwell-Boltzmann momentum distribution given by

$$n(\mathbf{k}) \;=\; \frac{N_\sigma}{\Omega} (4\pi\lambda\beta)^{d/2} \exp\left\{-\beta\lambda\mathbf{k}^2\right\} \;, \tag{15}$$

$$n(\mathbf{s}) \;=\; \exp\left\{-\frac{\mathbf{s}^2}{4\lambda\beta}\right\} \;. \tag{16}$$

The momentum distribution of an ideal Fermi gas with one spin state in 3 dimensions at $T = 0$ is a Fermi function,

$$n(\mathbf{k}) \;=\; \begin{cases} 1 & \text{for}\quad k \le k_F \\ 0 & \text{for}\quad k > k_F \end{cases} \quad \text{with}\;\; k_F = (6\pi^2 N_\sigma/\Omega)^{1/3} \tag{17}$$

$$n(\mathbf{s}) \;=\; 3/x^3 \left[\sin(x) - x\,\cos(x)\right] \;\text{with}\;\; x = s\,k_F \quad . \tag{18}$$

In this case, the free fermion SPRDM decays algebraically like $\cos(s\,k_F)/s^2$.

The probability distribution, $n(\mathbf{s})$, can be computed from PIMC simulations with one open path. The vector $\mathbf{s}$ is the separation of the two open ends. Methods developed for bosonic systems [2], such as liquid ^{4}He, carry over directly to fermionic path integrals, except for the nodal restriction.

During the PIMC simulations, $n(s)$ is recorded in form of a histogram. The separation of the open ends, s, of a particular configuration is added with the weight given by the sign of the permutation, $\mathbf{P}$. Even with the restriction, there are odd permutations that contribute to the Monte Carlo averages with negative weight. At separations where $n(s)$ is negative, odd permutations outweigh even permutations. The algebraic decay of $n(\mathbf{s})$ requires long exchange cycles, on the order of the number of particles. In restricted PIMC simulations, there is a direct relation [7] between long exchange cycles and the discontinuity of $n(k)$ at $k = k_F$.

2.3. Example of two free fermions

In order to illustrate the restricted path integral technique, we discuss the simplest fermionic system: the case of two identical fermions. The density matrix $\rho_{\rm T}(\mathbf{r}_1, \mathbf{r}_2, \mathbf{r}_1^*, \mathbf{r}_2^*; \beta)$ (Eq. 7) is positive if

$$(\mathbf{r}_1 - \mathbf{r}_2) \cdot (\mathbf{r}_1^* - \mathbf{r}_2^*) > 0. \tag{19}$$

For a given reference point, $(\mathbf{r}_1^*, \mathbf{r}_2^*)$, the nodal surface is a hyperplane given by $\mathbf{r}_1 = \mathbf{r}_2$ for all temperatures. This is illustrated in Fig. 1, which gives examples for the three types of paths that contribute to the sampling of diagonal density matrix elements. Paths that originate from the reference point, $(\mathbf{r}_1^*, \mathbf{r}_2^*)$, can either return to their point of origin or to the only possible permutation, $(\mathbf{r}_2^*, \mathbf{r}_1^*)$.
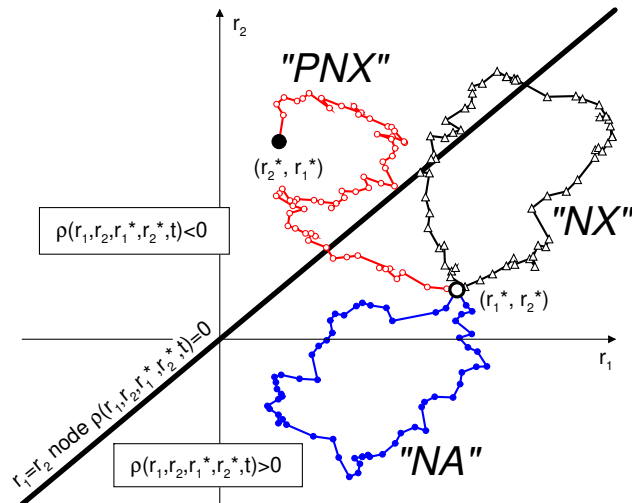
Figure 1: Illustration of the three different types of paths for two free fermions that originate from the reference point $(\mathbf{r}_1^*, \mathbf{r}_2^*)$. A node-avoiding ("NA"), a node-crossing ("NX") as well as a permuting and consequently node-crossing path ("PNX") are shown in the $(\mathbf{r}_1, \mathbf{r}_2)$ plane. The thick solid line indicates the node given by $\mathbf{r}_1 = \mathbf{r}_2$.

In restricted PIMC method, only node-avoiding paths labeled "NA" contribute. For two particles, the nodal restriction prohibits all permutations. However, if simulations with the *direct* fermion method are performed no restrictions are applied. Nonpermuting paths that cross the nodes ("NX") and those that avoid it ("NA") both enter with a positive sign. Permuting paths ("PNX") are now permitted and enter with a negative weight given by the $(-1)^{\mathcal{P}}$ factor. (In bosonic simulations, permuting and non-permuting paths enter with a positive weight.)

In order to compute the momentum distribution for two identical fermions, one would perform simulations with one open path. In case of the identity permutation, one polymer is open and the other one is closed. If the paths permute, one long polymer forms instead. Fig. 2 illustrates both cases in the $(\mathbf{r}_1, \mathbf{r}_2)$ plane. For simplicity, only paths that originate at $(\mathbf{r}_1^*, \mathbf{r}_2^*)$ and have an open end on the second coordinate, $\mathbf{r}_2$, are shown. Because of the nodal restriction only node avoid paths are shown: (*i*) Non-permuting paths with $\mathbf{r}_1 = \mathbf{r}_1^*$ and $\mathbf{r}_2 \neq \mathbf{r}_2^*$. The path of particle 1 is closed, that of particle 2 is open. (*ii*) Permuting paths with $\mathbf{r}_1 = \mathbf{r}_2^*$ and $\mathbf{r}_2 \neq \mathbf{r}_1^*$. When diagonal matrix elements are calculated, the nodal restriction eliminates the second type of paths because the final point, $(\mathbf{r}_2^*, \mathbf{r}_1^*)$, lies on the other side of the node. However, in simulations with open paths, many final points for permuting paths are permitted (see dashed line in Fig. 2) because path of particle 2 does not have to terminate at the origin of path of particle 1.

With increasing number of fermions, it becomes more difficult to illustrate the effects of the nodal restriction graphically. However, computationally the enforcement of the nodal restriction is not more difficult than for simulations with closed paths. One simply has to verify that the sign of the Slater determinant in Eq. (7) is positive $(\rho_T(\mathbf{R}(t), \mathbf{R}^*; \min(t, \beta - t)) > 0.)$ at every time step in imaginary time regardless whether
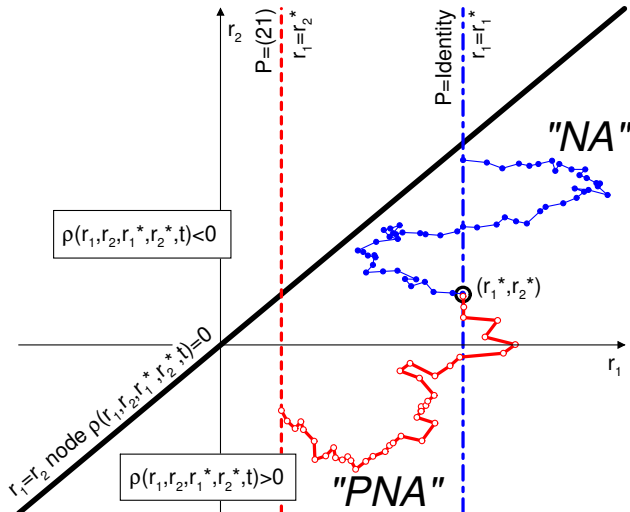
Figure 2: Illustration of node-avoiding paths that contribute to *off-diagonal* density matrix elements for two fermions. Both start at the reference point $(\mathbf{r}_1^*, \mathbf{r}_2^*)$. Shown are paths with one open end at r_2. The dot-dashed line indicates possible end points for nonpermuting paths [$\mathbf{r}_1 = \mathbf{r}_1^*$, labeled "NA"]. In contrast to on-diagonal matrix elements shown in Fig. 1, here, we find permuting but node-avoiding paths with end points on the dashed line [$\mathbf{r}_1 = \mathbf{r}_2^*$, labeled "PNA"] that represent negative contributions to the density matrix.

open paths are present in the simulations or not.

2.4. Monte Carlo sampling with open paths

When open paths are introduced to restricted PIMC simulations, one first has to decide at which point in imaginary time one opens the paths, relative to the reference point that one typically places at $t = 0$. With the dual reference point method, one can put the open ends at $t = 0$ or at $t = \beta/2$. We used the latter choice because it is more symmetric and one avoids the singular behavior of the fermion density matrices as $t \to 0^+$.

We used the bisection method [2] to sample new configurations of open and closed paths. First one first picks an interval in imaginary time of $2^l - 1$ steps, in which the paths will be regenerated. l is the number of bisection levels. If it is chosen too large, most trial moves will be rejected. If it is too small, the paths diffuse very slowly. The optimal choice depends on strength of the interactions and the fermion degeneracy. After selecting the time interval, one uses the heat-bath algorithm to sample permutation space of the moving particles. One proceeds with the bisection method until new positions have been proposed at every time step. In this study, we sample the paths from the free-particle density matrix. For a closed path that connects points $\mathbf{r}_1$ and $\mathbf{r}_2$, the sampling probability becomes,

$$T_l(\mathbf{r}) = (2^l \pi \lambda \tau)^{d/2} \exp\left\{ -\frac{(\mathbf{r} - \mathbf{r}_\mathrm{m})^2}{2^l \lambda \tau} \right\} \quad , \tag{20}$$

where $\mathbf{r}_\mathrm{m}$ is the mid point $(\mathbf{r}_1+\mathbf{r}_2)/2$. For strongly interacting systems, a better sampling efficiency has been reached by adding a drift and a covariance term [2]. The free-particle sampling probability of an open path that is connected at one point $\mathbf{r}_1$ reads,

$$T_l(\mathbf{r}) = (4^l \pi \lambda \tau)^{d/2} \exp\left\{ -\frac{(\mathbf{r} - \mathbf{r}_1)^2}{4^l \lambda \tau} \right\} \quad . \tag{21}$$

The pair action, $u(\mathbf{R}, \mathbf{R}'; \beta) = -\log[\rho(\mathbf{R}, \mathbf{R}'; \tau)/\rho_0(\mathbf{R}, \mathbf{R}'; \tau)]$, is then used to determine whether a particular configuration will be rejected or preliminarily accepted.

As a final step, one verifies if the nodal constraint is satisfied at every time step. Otherwise the proposed configuration is rejected. For fermion simulations with only closed paths, one can eliminate odd permutations from consideration because they would inevitably violate the nodes. In the presence of open paths, this is no longer correct because otherwise we would not be able to sample the negative pieces of the SPRDM. Still in simulations with open path the following two conditions can be used to eliminate paths early on that violate the nodes: (a) It is impossible to permute an even number of closed paths while keeping the coordinates of all other particles fixed. (b) It is impossible to permute an open and a closed path in a move that does not change the time slice with the open ends. These two simple rules are employed to improve the efficiency of the algorithm. Paths that violated these conditions would inevitably be rejected lagter when the nodal restriction are enforced rigorously.

In a homogeneous system, the SPRDM $n(\mathbf{s})$ is only a function of $|\mathbf{s}|$. However, in a periodic but finite simulation cell, $n(\mathbf{s})$ is expected show some dependence on the orientation of $\mathbf{s}$ vector with respect to the cell vectors. Still all $n(s)$ results, that we will be present, will be spherically averaged. However, for the computation of the momentum distribution, $n(\mathbf{k}) \propto \langle e^{i\mathbf{k}\mathbf{s}} \rangle$, the angular dependence of $n(\mathbf{s})$ is important. Therefore we compute $n(\mathbf{k})$ directly during the Monte Carlo simulation for a reasonable number of $\mathbf{k}$ vectors. This avoids storing averages of the d dimensional function $n(\mathbf{s})$.

The normalization of $n(s)$, is not determined *a priori* in the PIMC simulations. Like for bosonic simulations, we determine the normalization by anchoring the distribution at the origin, $n(s = 0) = 1$. To further reduce the error bars of $n(s)$, we sample the open path more often than the others and increase the frequency of moves that involve the open slice. Still, a difficulty arises from the fact that the probability for the two open ends to be separated by less than distance δ scales as δ^d in d dimensions. The associated statistical uncertainty increases for small δ as $\delta^{-d/2}$, which makes it difficult to anchor the distribution $n(s)$ accurately. To make this process more robust, we fit the observed histogram of end-to-end separations, s, to the following functional form:

$$\lim_{s \to 0} n_\mathrm{MC}(s) = \xi_1 \left[1 - \frac{\langle K \rangle}{\lambda d} s^2 + \xi_2 s^4 \right] \quad . \tag{22}$$

ξ_1 and ξ_2 are fit parameters. K is the kinetic energy of the system that we computed with separate simulations of only closed paths.

3. Results

We determined the momentum distribution of the homogeneous electron gas at three different conditions. First we study the spin polarized electron gas at a density of $r_s =$
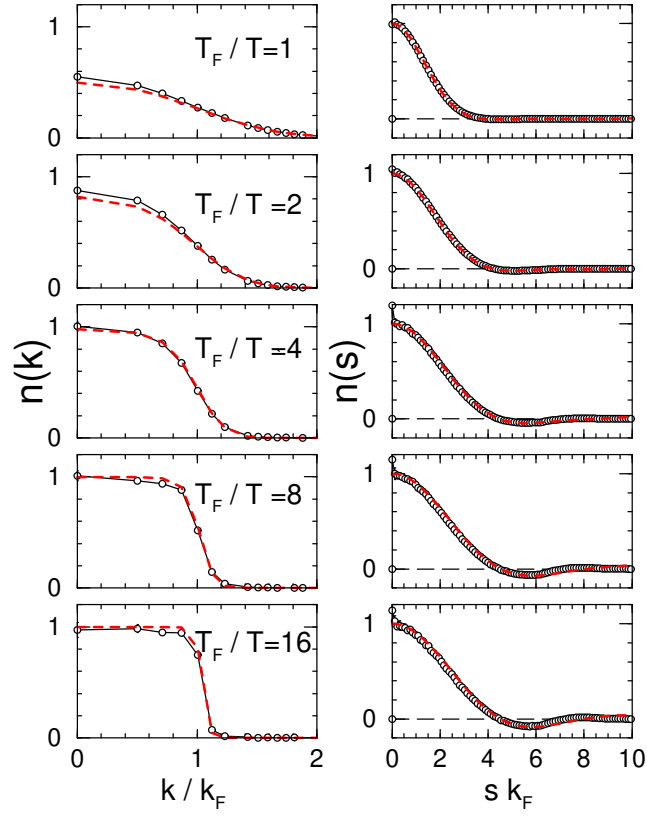
9

Figure 3: The left panels show the momentum distributions $n(k)$ from PIMC simulations (circles) with 33 spin polarized electrons for different temperatures at ($r_s = 4$). For $T \geq T_F/4$, the population of low momentum states is enhanced compared with the corresponding ideal Fermion results (dashed lines), which leads to a lowering of kinetic energy ($K < K_0$). The right panel shows the corresponding off-diagonal density matrix elements $n(s)$. With decreasing temperature, a negative region near $sk_F = 5.8$ appears.
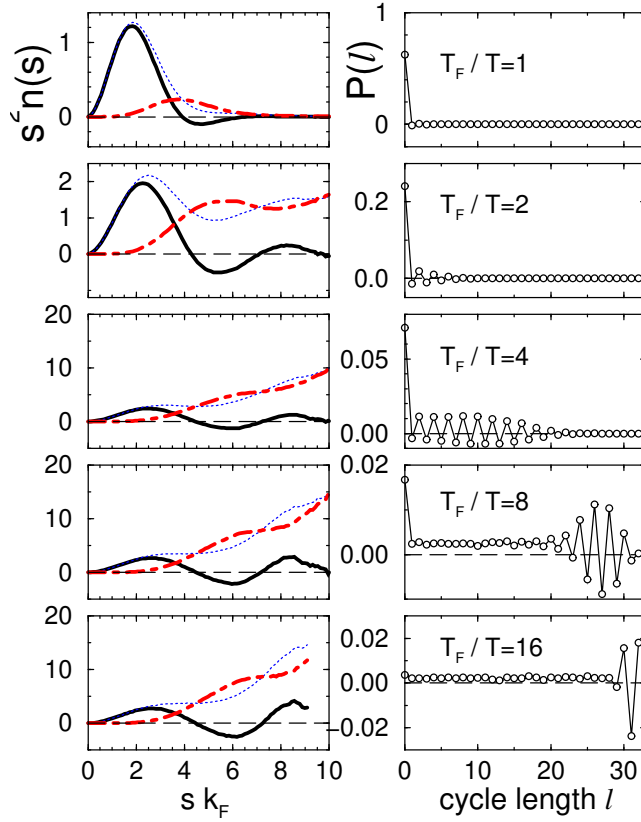
Figure 4: The left panels shows the distribution of the open ends, $n(s)$ multiplied by the volume element s^2 (solid lines) for a system of 33 spin polarized electrons for $r_s = 4$ and different temperatures that correspond to those in Fig. 3. The dash-dotted lines indicate the distribution of paths that enter with a negative sign. Their contribution vanishes more quickly for small s because they do not contribute to diagonal elements of density matrix ($s = 0$). The dashed lines represent the remaining positive contributions. The right column shows the distribution of permutation cycles as a function of cycle length l.
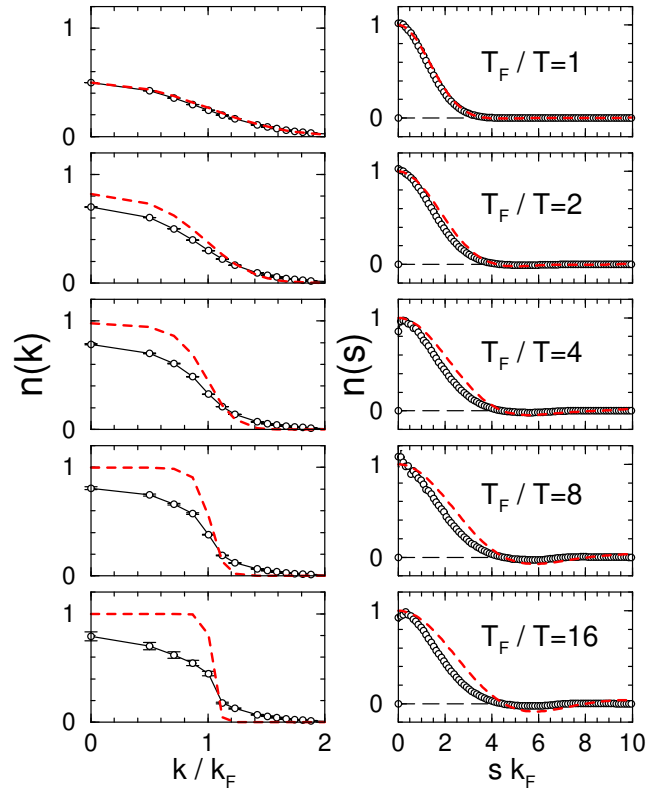
Figure 5: Momentum distribution $n(k)$ and off-diagonal density matrix $n(r)$ for the spin polarized electron gas at $r_s = 40$ from simulations with 33 particles. Deviations from the ideal Fermion results are increased compared to Fig. 3 (see description and line styles there) due to increased correlation effects.
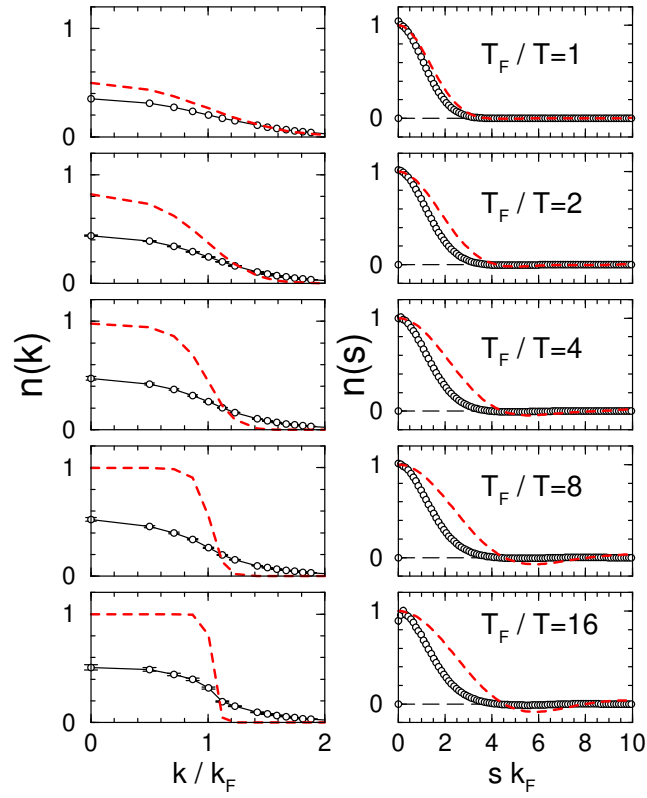
12

Figure 6: Momentum distribution $n(k)$ and off-diagonal density matrix $n(r)$ function for the unpolarized electron gas at $r_s = 40$ from simulations with 66 particles. Correlation effects are enhanced compared to Figs. 3 and 5 (see description and line styles there).
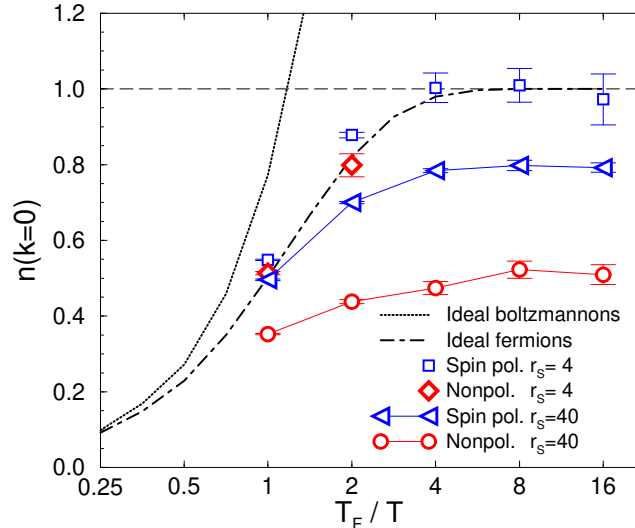
Figure 7: The temperature dependence of the population of the zero momentum state, $n(k = 0)$, is shown for two densities ($r_s = 4$ and 40) of the fully spin polarized electron gas (from PIMC simulations with 33 particles) and for the nonpolarized case (simulations with 66 particles).

4, which corresponds to the electron density of a low density metal such as sodium. The computed momentum distribution turns is similar to that of an ideal Fermi gas. Second we calculated $n(k)$ for spin polarized electron gas at a much lower density of $r_s = 40$, where correlation effects are very large and significant deviations from the free particle behavior are found. Finally we present results for the nonpolarized electron gas at $r_s = 40$ where correlation effects are even more important. For all three conditions, we have computed the momentum distribution for a series of temperatures ranging from $1 \leq T_F/T \leq 16$. We compare with results from zero temperature quantum Monte Carlo simulations.

Fig. 3 shows the momentum distribution for spin polarized electron gas as a function of temperature. In the limit of high temperature $T \gg T_F$, fermion effects become less important and one recovers the classical Maxwell-Boltzmann distribution. With decreasing temperature, one finds that population of low momentum states with $k < k_F$ increases until it reaches 1, the maximum allowed by the Pauli exclusion principle. Simultaneously, the slope of $n(k)$ at the Fermi wave vector becomes increasingly steep. We do not exactly recover the limit of ideal Fermi function in Eq. 17, because of finite size effects. The system size we used, $N = 33$ at $T = T_F/16$, is already a demanding computation, in part because we used a time step of $\tau = 1/32T_F$ needed to enforce the nodal constraint accurately along the paths that required simulations with up to 384 time slices. Notice that at $T = T_F/16$ there are still small but non-negligible thermal excitations of states above k_F present. The correlation effects, absent for free particles, are small but nevertheless significant. At high temperature, the interactions lead to an increased population of low momentum states resulting in a lowering of the total kinetic energy. The reason for this effect is that the entropy is the dominant part of the free

14

energy at high temperature. Interactions can lower the entropy which also leads to a lowering of the kinetic energy. This effect has been discussed in detail in [39]. At low temperature, the free energy is dominated by the interaction term and the kinetic energy is always higher than the corresponding ideal value. As a result, even at $T = 0$, states above the k_F are populated. According to Migdal's theorem [40], as long as the system remains a Fermi liquid, the discontinuity at k_F remains, but the step size is reduced compared to the free fermion value.

On the right side of Fig. 3, we show the SPRDM $n(s)$. They are very close to the corresponding free particles distributions. However, in the more correlated systems, discussed later, significant deviations from the ideal behavior are found. At high temperature, (in the classical limit) $n(s)$ is dominated by a single Gaussian. With decreasing temperature, a shallow negative region develops around $sk_F = 5.8$. At $sk_F = 7.25$, $n(s)$ becomes positive again and exhibits a maximum at $sk_F = 8$. Further oscillations cannot be identified for this system size.

Fig. 4 shows the distribution of positive and negative contribution of the SPRDM. At small separation, $n(s)$ is dominated by the positive contributions because negative terms are strongly disfavored by the nodal restriction. The negative region near $sk_F = 5.8$ develops because two particle permutations occur with increasing probability for temperatures $T \leq T_F$. Such open paths can spread out further than single open paths and therefore start to dominate at intermediate separations, s. As the temperature is decreased further below T_F, longer and longer permutation cycles contribute to $n(s)$. The magnitude of positive and negative contributions increases with s but each function dominates for different separations giving rise to the oscillatory behavior of the total $n(s)$ function, which is expected from the zero temperature result.

Fig. 4 also shows the probability of finding a permutation cycle, $P(l)$, weighted the overall permutation sign as a function of the cycle length. At high temperature longer permutation cycles occur with very small probability because the thermal De Broglie wave length, $\lambda_{\text{th}}^2 = 4\pi\lambda\beta$, is short compared to the inter-particle spacing, which renders permutations unlikely. With decreasing temperature, longer permutations occur more frequently and the cycle distribution approaches a positive constant at $T = T_F/8$. The occurrence of a particular cycle length is no longer correlated with total permutation, and overall there are more positive than negative permutations. At lower temperature $T = T_F/16$, more negative permutations occur, which reduces the function $P(l)$. qThis distribution shows oscillation for the largest occurring cycle lengths, which is a finite size effect. When such a long cycle occurs it is less likely there is also another permutation cycle that alters the total sign of the permutation.

Fig. 5 shows the $n(k)$ and $n(s)$ functions for the spin polarized electron gas at a much lower density of $r_s = 40$. Under these conditions, the particles are significantly more correlated and their behavior differs substantially from that of free fermions. As a result, the momentum distribution is much more spread out leading to the population of higher momentum states. The total kinetic energy is clearly above the corresponding ideal value. In the low temperature limit, the population of the $k = 0$ state reaches a value of only about 0.8 compared to 1.0 for free particles. The $n(s)$ distribution is shifted to smaller s values indicating that the paths are more localized because of repulsive interactions.

Fig. 6 shows the corresponding results for the nonpolarized electron gas with 66 electrons. These simulations are much more efficient than simulations at higher density because the interactions lead to some localization, which cuts down on the number of long

permutation cycles that need to samples accurately. Simulations of stronly correlated systems are therefore less demanding than those of weakly interacting particles.
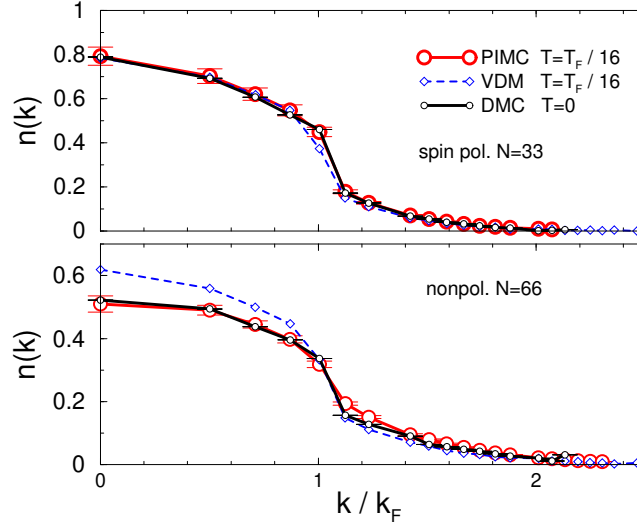

Figure 8: Comparison of the momentum distribution for $r_s = 40$ at $T = T_F/16$ computed with PIMC, VDM and ground state diffusion Monte Carlo (DMC) calculations at $T = 0$. The upper graph shows results from simulation with 33 spin polarized electrons, the lower graph represents the unpolarized case with 66 particles.

In Fig. 7, the occupation of the zero momentum state is plotted as a function of temperature. At high temperature, all curves converge to the free particle result. Simulations of the spin polarized electron gas at $r_s = 4$ are above the ideal result for high temperatures underlining the lowering of the kinetic energy. For low temperatures, they converge to the ideal value of 1 within the error bars. The graph also shows that the low density results converge to a ground state limit as well.

In Fig. 8, we compare PIMC results at $T = T_F/16$ with the ground state momentum distribution derived from diffusion Monte Carlo (DMC) simulations using backflow nodes [41] (For additional DMC results see [42]). The agreement between PIMC and DMC is excellent for both spin polarizations considered here. Only for the unpolarized case, one observes some very small deviations around $k \approx k_F$, an indication of thermal excitation present.

Fig. 8 for the spin polarized case shows good agreement with a variational density matrix (VDM) calculation using the free particle density matrix (Eq. 7) multiplied by a temperature dependent pair product Jastrow factor. The Jastrow factors had the form,

$$j(\mathbf{r}, \mathbf{r}'; \beta) = \exp\left[-\frac{P(\mathbf{r}; \beta) + P(\mathbf{r}'; \beta)}{2}\right] , \qquad (23)$$

with $P(\mathbf{r}; \beta) = A(1 - e^{-Br})/r$. To satisfy the cusp condition at the origin and the free plasmon large r limit, $A = 2\sqrt{r_s^3/3}\tanh(\frac{\beta}{2}\sqrt{3/r_s^3})$ and $B = \sqrt{2/A}$. This trial density matrix reproduces the known ground state correlation energies to a relative accuracy of
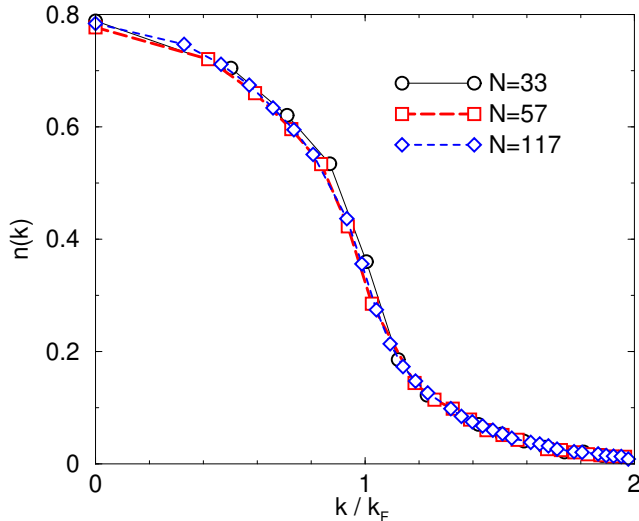
16

Figure 9: Finite size study of the momentum distribution for spin polarized electron gas at $r_s = 40$ and $T_F/T = 8$ computed using the variational density matrix method for $N = 33$, 57, and 117 particles in periodic boundary conditions.

4% for $r_s = 1$ to 20 and correctly approaches the high temperature limit. However for the unpolarized, VDM predicts $n(k)$ values that are significantly too high for $k < k_F$. While the VDM method can certainly be improved by choosing parameters in the Jastrow factor more appropriately, it underlines the need for methods such as restricted PIMC simulations that work without input from analytical calculations.

To estimate the finite size effects, we used the VDM method which is significantly less computationally demanding than PIMC simulations. Fig. 9 shows the finite size dependence of the momentum distribution for the spin polarized electron gas at $r_s = 40$ and $T_F/T = 8$, a density at which PIMC and VDM agree well. The simulations were performed for different numbers of particles corresponding to filled k shell structures with $N = 33$, 57, and 117 particles. Using periodic boundary conditions, the function $n(k)$ can only be computed for k values in the reciprocal lattice of the simulation cell. Consequently, $n(k)$ is shown for a different set of k values depending on the number of particles. The overall agreement of the computed momentum distribution is very good, indicating that the finite size errors are small at these temperatures.

4. Conclusions

This computational technique allows one to calculate the momentum distribution within PIMC for fermion systems. It combines the sampling methods using open paths developed for bosonic liquids with restricted path technique derived for fermions. Results for the homogeneous electron gas show that the temperature dependence of the momentum distribution can be studied and ground state results can be reproduced. The method is applicable to any Fermi system, in particular to hot dense hydrogen [43] where

17

one expects significant changes in the momentum distribution with increasing density as the electrons are delocalized in the molecular-metallic transition, and to calculate the momentum distribution of ^{3}He [44] and ^{3}He-^{4}He mixtures.

Acknowledgments

[1] G. Baym, "Lectures On Quantum Mechanics", The Benjamin/Cummings Publishing Company, San Francisco, CA, USA, 1969.
[2] D. M. Ceperley, Rev. Mod. Phys. 67 (1995) 279.
[3] M. Holzmann, B. Bernu, C. Pierleoni, J. McMinis, D. M. Ceperley, V. Olevano, L. D. Site, Phys. Rev. Lett. 107 (2011) 110402.
[4] E. Pollock, D. M. Ceperley, Phys. Rev. B 30 (1984) 2555.
[5] D. M. Ceperley, Phys. Rev. Lett. 69 (1992) 331.
[6] C. Pierleoni, D. Ceperley, B. Bernu, W. Magro, Phys. Rev. Lett. 73 (1994) 2145.
[7] D. M. Ceperley, in: E. K. Binder, G. Ciccotti (Eds.), Monte Carlo and Molecular Dynamics of Condensed Matter Systems, Editrice Compositori, Bologna, Italy, 1996.
[8] W. R. Magro, D. M. Ceperley, C. Pierleoni, B. Bernu, Phys. Rev. Lett. 76 (1996) 1240.
[9] B. Militzer, W. Magro, D. Ceperley, Contr. Plasma Physics 39 1-2 (1999) 152.
[10] B. Militzer, D. M. Ceperley, Phys. Rev. Lett. 85 (2000) 1890.
[11] B. Militzer, D. M. Ceperley, Phys. Rev. E 63 (2001) 066404.
[12] B. Militzer, D. M. Ceperley, J. D. Kress, J. D. Johnson, L. A. Collins, S. Mazevet, Phys. Rev. Lett. 87 (2001) 275502.
[13] B. Militzer, Phys. Rev. Lett. 97 (2006) 175501.
[14] B. Militzer, Phys. Rev. B 79 (2009) 155105.
[15] B. Militzer, J Phys. A 42 (2009) 214001.
[16] B. Militzer, J. Low Temp. Phys. 139 (2005) 739.
[17] M. D. Jones, D. M. Ceperley, Phys. Rev. Lett. 76 (1996) 4572.
[18] E. L. Pollock, B. Militzer, Phys. Rev. Lett. 92 (2004) 021101.
[19] B. Militzer, E. L. Pollock, Phys. Rev. B 71 (2005) 134303.
[20] E. W. Brown, B. K. Clark, J. L. DuBois, D. M. Ceperley, Path-Integral Monte Carlo Simulations of the Warm Dense Homogeneous Electron Gas, Phys. Rev. Lett. 110 (2013) 146405.
[21] T. Schoof, S. Groth, J. Vorberger, M. Bonitz, Ab initio thermodynamic results for the degenerate electron gas at finite temperature, Phys. Rev. Lett. 115 (2015) 130402.
[22] S. Groth, T. Dornheim, T. Sjostrom, F. D. Malone, W. M. C. Foulkes, M. Bonitz, Ab initio exchange-correlation free energy of the uniform electron gas at warm dense matter conditions, Phys. Rev. Lett. 119 (2017) 135001.
[23] F. D. Malone, N. S. Blunt, E. W. Brown, D. K. K. Lee, J. S. Spencer, W. M. C. Foulkes, J. J. Shepherd, Accurate exchange-correlation energies for the warm dense electron gas, Phys. Rev. Lett. 117 (2016) 115701.
[24] L. X. Benedict, K. P. Driver, S. Hamel, B. Militzer, T. Qi, A. A. Correa, A. Saul, E. Schwegler, A multiphase equation of state for carbon addressing high pressures and temperatures, Phys. Rev. B 89 (2014) 224109.
[25] K. P. Driver, B. Militzer, Phys. Rev. B 93 (2016) 064101.
[26] K. P. Driver, B. Militzer, Phys. Rev. E 95 (2017) 043205.
[27] S. Zhang, K. P. Driver, F. Soubiran, B. Militzer, Phys. Rev. E 96 (2017) 013204.
[28] S. Zhang, B. Militzer, L. X. Benedict, F. Soubiran, P. Sterne, K. P. Driver, J. Chem. Phys. 148 (2018) 102318.
[29] S. Zhang, B. Militzer, M. C. Gregor, K. Caspersen, L. H. Yang, T. Ogitsu, D. Swift, A. Lazicki, D. Erskine, R. A. London, P. M. Celliers, J. Nilsen, P. A. Sterne, H. D. Whitley, Phys. Rev. E 98 (2018) 023205.
[30] B. Militzer, K. P. Driver, Phys. Rev. Lett. 115 (2015) 176403.
[31] S. X. Hu, B. Militzer, L. A. Collins, K. P. Driver, J. D. Kress, Phys. Rev. B 94 (2016) 094109.
[32] S. Zhang, K. P. D. F. Soubiran, B. Militzer, J. Chem. Phys. 146 (2017) 074505.

[33] K. P. Driver, F. Soubiran, B. Militzer, Phys. Rev. E 97 (2018) 063207.

[34] V. Natoli, D. M. Ceperley, J. Comp. Phys. 117 (1995) 171–178.

[35] B. Militzer, Computation of the high temperature coulomb density matrix in periodic boundary conditions, Comp. Phys. Comm. 204 (2016) 88.

[36] E. Pollock, D. M. Ceperley, Phys. Rev. B 36 (1987) 8343.

[37] D. M. Ceperley, J. Stat. Phys. 63 (1991) 1237.

[38] B. Militzer, E. L. Pollock, Phys. Rev. E 61 (2000) 3470.

[39] B. Militzer, E. L. Pollock, Phys. Rev. Lett. 89 (2002) 280401.

[40] A. B. Migdal, JETP 5 (1957) 333.

[41] F. H. Zong, C. Lin, D. M. Ceperley, Phys. Rev. E 66 (2002) 036703.

[42] G. Ortiz, P. Ballone, Phys. Rev. B 50 (1994) 1391.

[43] S. Weir, A. Mitchell, W. Nellis, Phys. Rev. Lett. 76 (1996) 1860.

[44] R. Senesi, C. Andreani, D. Colognesi, A. Cunsolo, M. Nardone, Phys. Rev. Lett. 86 (2001) 4584.